Li Huang, Gerd Mikolajczyk, Ekkehard Küstermann, Michaela Wilhelm, Stefan Odenbach, Wolfgang Dreher

Adapted MR velocimetry of slow liquid flow in porous media

Journal Article	as:	peer-reviewed accepted version (Postprint)
DOI of this document*(secondary publication):		https://doi.org/10.26092/elib/2499
Publication date of this document:		29/09/2023

* for better findability or for reliable citation

Recommended Citation (primary publication/Version of Record) incl. DOI:

Li Huang, Gerd Mikolajczyk, Ekkehard Küstermann, Michaela Wilhelm, Stefan Odenbach, Wolfgang Dreher,
Adapted MR velocimetry of slow liquid flow in porous media,
Journal of Magnetic Resonance, Volume 276, 2017, Pages 103-112, ISSN 1090-7807,
https://doi.org/10.1016/j.jmr.2017.01.017

Adapted MR velocimetry of slow liquid flow in porous media

Li Huang [a,*], Gerd Mikolajczyk [b], Ekkehard Küstermann [a], Michaela Wilhelm [c], Stefan Odenbach [b], Wolfgang Dreher [a]

[a] In-vivo-MR Group, Faculty 02 (Biology/ Chemistry), University of Bremen, 28359 Bremen, Germany
[b] Chair of Magnetofluiddynamics, Measuring and Automation Technology, Institute of Fluid Mechanics, Technical University of Dresden, 01062 Dresden, Germany
[c] Advanced Ceramics Group, Faculty 04 (Production Engineering - Mechanical Engineering and Process Engineering), University of Bremen, 28359 Bremen, Germany

ARTICLE INFO

Article history:
Received 8 December 2016
Revised 24 January 2017
Accepted 25 January 2017
Available online 27 January 2017

Keywords:
MR velocimetry
Phase contrast MRI
Quantitative MRI
Porous media
RF coil
MR pulse sequence
RARE

ABSTRACT

MR velocimetry of liquid flow in opaque porous filters may play an important role in better understanding the mechanisms of deep bed filtration. With this knowledge, the efficiency of separating the suspended solid particles from the vertically flowing liquid can be improved, and thus a wide range of industrial applications such as wastewater treatment and desalination can be optimized. However, MR velocimetry is challenging for such studies due to the low velocities, the severe B_0 inhomogeneity in porous structures, and the demand for high spatial resolution and an appropriate total measurement time during which the particle deposition will change velocities only marginally. In this work, a modified RARE-based MR velocimetry method is proposed to address these issues for velocity mapping on a deep bed filtration cell. A dedicated RF coil with a high filling factor is constructed considering the limited space available for the vertical cell in a horizontal MR magnet. Several means are applied to optimize the phase contrast RARE MRI pulse sequence for accurately measuring the phase contrast in a long echo train, even in the case of a low B_1 homogeneity. Two means are of particular importance. One uses data acquired with zero flow to correct the phase contrast offsets from gradient imperfections, and the other combines the phase contrast from signals of both odd and even echoes. Results obtained on a 7T preclinical MR scanner indicate that the low velocities in the heterogeneous system can be correctly quantified with high spatial resolution and an adequate total measurement time, enabling future studies on flow during the filtration process.

1. Introduction

Deep bed filtration [1–5] is a separation process with the aim of clarifying a liquid. To this end, the liquid with suspended solid particles is slowly streaming downwards through the porous filter with local velocities of submillimeters to millimeters per second. Two groups of mechanisms underlie the filtration process, one leads to routes of particles towards interfaces between the liquid and the porous filter (*e.g.* gravity settling, diffusion, interception), and the other causes immobilization of particles at the filter surfaces (Van-der-Waals and electrostatic forces, straining). Due to the large amount of particles which can be retained and the slow increase of pressure drop, deep bed filtration is widely used in industrial applications, such as wastewater treatment and desalination [4,5].

Recent studies [6–14] have shown the potential of X-ray *Micro-Computed Tomography* (μCT) for characterizing the particle deposition processes. With 3D spatial resolution in the micrometer to submillimeter range, serial X-ray μCT images of porous structures and deposited particles over time can provide microscopic knowledge of the particle deposition processes.

While the correlation between the particle deposition processes and the velocity fields of the flowing liquid has been studied for other filtration processes [15–17], this correlation has not been studied yet for deep bed filtration. Insights into this correlation will certainly lead to a more profound understanding of deep bed filtration mechanisms and thus an improved design of deep bed filters with regard to filtration efficiency. Quantifying the velocity fields of the liquid can be achieved by *MR Velocimetry* (MRV) [18,19], which is particularly preferred for opaque structures, where optical velocimetry techniques cannot be applied. MRV is a highly versatile tool for velocity mapping of fluid flow, since it contains a variety of adaptable methods for laminar and turbulent, single-phase and multi-phase, fast and slow flow [18,19]. For the specific case of deep bed filtration, dedicated MRV is required for measuring slow liquid flow of submillimeters to millimeters per second in macroporous media with 3D sub-pore-scale spatial resolution.

* Corresponding author.
E-mail address: lhuang@uni-bremen.de (L. Huang).

http://dx.doi.org/10.1016/j.jmr.2017.01.017
1090-7807/

Additionally, this MRV method should allow an adequate total measurement time, because the velocity fields of the liquid can alter significantly due to substantial changes of pore filling after a few hours of filtration.

MRV can be achieved by adding a displacement encoding module to a standard MRI pulse sequence. There are two main MRV methods, *q-space* MRI [20] and *phase contrast* MRI [21–23]. In q-space MRI, the probability distribution of fluid displacements is spatially resolved as voxel-wise propagator spectra. In phase contrast MRI, the voxel-wise average propagator is directly measured to provide the average fluid displacement within each voxel. Though inferior in velocimetry accuracy to q-space MRI, phase contrast MRI is widely used due to the much smaller number of required displacement encoding steps, leading to a shorter minimum total measurement time.

In phase contrast MRI, the *Signal-to-Noise Ratio* (SNR) of the complex-valued MR images is not only a measure of image quality, but also determines the accuracy of measured velocity maps, because the *STandard Deviation* (STD) of the velocities is reciprocally proportional to the SNR [24–26]. Therefore, phase contrast MRI methods using a *Spin Echo* (SE) based magnetization preparation module for velocity encoding are superior to those using a STimulated Echo (STE) based magnetization preparation module, because the latter implies a general 50% signal loss.

MRV can be accelerated by different methods, *e.g.*, compressed sensing, Bayesian MR, and parallel imaging [19]. Another strategy with respect to MRI pulse sequence design is the use of multiple echoes for multiple phase encoding steps, *i.e.* the *Rapid Acquisition with Relaxation Enhancement* (RARE) method [27]. RARE MRV is a reasonably fast MRV approach [28–37] and has been applied for displacement mapping of liquid in porous systems like plants [28,29] and rocks [37].

A recent study [37] showed that RARE phase contrast MRI with 3D super-pore-scale spatial resolution can still be accurate for very slow liquid flow in porous media. However, the implementation of the method in [37] was not considered optimal for the current work. First, a specific STE based magnetization preparation module [38] was used in [37] due to very small velocities of submillimeters per second and strong internal magnetic field gradients within each super-pore-scale voxel, while an SE based magnetization preparation module can be used in the current work to improve the SNR because of relatively larger velocities and weaker internal magnetic field gradients within each sub-pore-scale voxel. Second, a rather small RARE factor (2) and thus a short echo train length were used in that study due to short T_2 in rocks, while longer T_2 in deep bed filters enables a larger RARE factor. However, several additional strategies need to be considered for velocimetry accuracy with a relatively longer echo train length, such as RF filtering [34] or phase cycling [33,36] for recovering the correct complex-valued signals, as well as phase encoding winder and rewinder gradients for suppressing motion artifacts.

In this work, an efficient and accurate MRV approach for slow liquid flow in porous media was achieved by adapting existing RARE phase contrast MRI methods. For SNR reason and due to a moderate velocity range to be measured, an SE based velocity encoding module was used. A two-step phase cycling containing CPMG and CP pulse trains [33,36] was applied to preserve the propagator information within the magnetization in the echo train. Velocity offsets caused by gradient imperfections [39–41] were measured with zero flow for correcting the velocity maps of the flowing liquid. Velocity maps of odd and even echoes in the echo train were combined to increase velocimetry accuracy. The proposed MRV approach can be a helpful tool for improving the understanding of deep bed filtration and may also be of interest for further MRV applications.

2. Methods

2.1. Porous filter sample

A templated foam derived from polysiloxane was produced as a cylindrical filter sample (diameter 9 mm, height 18 mm) with spherical pores with a mean diameter of about 2 mm according to [42]. Expanded polystyrene beads (~2 mm, Klassen Vitali, Germany) were used as templates and packed in a poly-propylene mold. This mold was infiltrated with a mixture of 86 wt% of methyl phenyl polysiloxane (H44, Wacker Chemie AG, Germany) and 14 wt % of 3-aminopropyltriethoxysilane (APTES, abcr GmbH, Germany) in a few milliliters of ethanol. The beads packing in the originally completely filled mold was compressed by 6.25 vol%, while excessive polymer solution was drained. After cross-linking at room temperature and 100 °C, the pyrolytic conversion of the cross-linked material was carried out at 1000 °C under nitrogen. This SiOC ceramic was shown to have a hydrophilic surface characteristic by performing water and n-heptane adsorption experiments.

Distilled water was used as the liquid flowing through the sample. The sample was mounted in a dedicated filtration cell made of polytetrafluoroethene (PTFE). The inlet and outlet in the filtration cell have an inner diameter of 8 mm. The filtration cell was connected to a peristaltic tubing pump (ISMATEC REGLO Analog MS-2/6, Cole-Parmer GmbH, Germany) by tubes. The pump permits steady liquid flow through the filtration cell with the linearly controllable *Volumetric Flow Rate* (VFR) between 1.26 and 125 mm^3/s. The linearity and the VFR range were measured by monitoring the volume of the distilled water flowing out of the filtration cell. Due to the long tube length between the pump and the filtration cell (>3 m), the pulsation effect of the peristaltic pump is regarded as negligible. Before MR experiments, the filtration cell was soaked within the distilled water in the bottom part of a desiccator to achieve pore pre-saturation, and then the desiccator was sealed and evacuated from the top by a vacuum pump for pore saturation. Due to the low pressure, remaining gas within the pores degassed and the pores were eventually saturated.

2.2. MR hardware

All MR experiments were performed on a horizontal 7T scanner (BioSpec 70/20 USR, Bruker BioSpin MRI GmbH, Germany), which is equipped with a 114 mm bore gradient system (B-GA 12S2, Bruker BioSpin MRI GmbH, Germany) and controlled by ParaVision 5.1 (Bruker BioSpin MRI GmbH, Germany) on a Linux workstation. The gradient system contains room temperature shim coils of up to second-order, a maximum gradient amplitude of 440 mT/m and a maximum slew rate of 3440 mT/m/ms.

Due to the vertically orientated filtration in deep bed filters, a vertical MR scanner would certainly be a good choice. However, the drawback of limited vertical space available in a horizontal MR scanner with a horizontal RF coil was reduced by using a home-made, vertically orientated RF coil. This dedicated coil consists of two identical thin rectangular copper plates fixed on the outer surface of a hollow PTFE cylinder resulting in a loop-gap resonator. A fixed-value capacitor was soldered on one gap and a trimmer capacitor on the other gap to link the two copper plates. A pick-up loop covering the resonator bore was mounted on a PTFE slider, which supports the movement of the pick-up loop along the longitudinal direction of the loop-gap resonator. Tuning and matching of this linear transceiver RF coil is performed by adjusting the trimmer capacitor and sliding the pick-up loop longitudinally, respectively.

In order to achieve high RF efficiency and SNR, the filling factor of the coil was maximized by adapting the resonator diameter to

the filtration cell diameter. The cylindrical resonator body and the pick-up loop slider were manufactured of PTFE, in order to avoid background signals originating from proton-containing materials.

The coil used in this work has a diameter of 22 mm and a height of 25 mm. B_1 mapping by the *Double Angle Method* [43] was performed on a static water tube with the maximum filling factor of the coil. Across the expected FOV, which is the central region in the filtration cell, the B_1 inhomogeneity of the coil was shown to range from −57% to +14% (*cf.* supplementary material 1). For comparison and initial methodological developments, some experiments were performed by using a commercial horizontal 72 mm bore birdcage ^{1}H quadrature transceiver RF coil (Bruker BioSpin MRI GmbH, Germany).

2.3. MRI pulse sequence

The proposed RARE phase contrast MRI pulse sequence is schematically shown in Fig. 1, where τ is the delay between the excitation and the first refocusing pulses, g is the amplitude of the velocity encoding gradient, δ is the duration of the velocity encoding gradient, and Δ is the delay between the velocity encoding gradients. A velocity encoding module with a pair of unipolar gradients separated by a refocusing pulse is placed after the excitation pulse for magnetization preparation. The velocity encoding gradients can be applied in arbitrary direction. By inverting the polarity of the velocity encoding gradients, displacements are encoded into the phase of the MR signals. For 3D velocimetry, an Hadamard scheme [44,45] defines the polarities of velocity encoding gradients in three orthogonal directions, as shown in Table 1. The velocity encoding range is defined as [-VENC,VENC], covering the *Field of Flow* of 2·VENC, where the *Velocity ENCoding* (VENC) is given by

$$VENC = \frac{\pi}{N_V \gamma g \delta \Delta}, \tag{1}$$

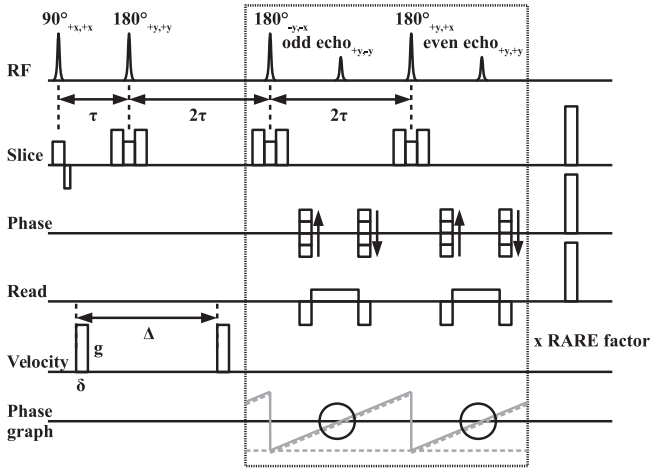

Fig. 1. The RARE phase contrast MRI pulse sequence for 2D imaging with 1D velocimetry, applied with centric phase encoding. The echo after the first refocusing pulse in the preparation module, which will be formed only if gradient recall is done by a second velocity encoding gradient before this echo, is not acquired and thus not shown in the diagram. A pair of an odd echo and the subsequent even echo experiences identical spatial encoding gradients, *i.e.* phase encoding gradients are incremented after every pair of odd and even echoes. For non-slice-selective 3D imaging, soft RF pulses with slice-selection and slice-rephasing gradients are replaced by hard RF pulses, and phase encoding is also performed in the slice direction. The velocity encoding can be performed in arbitrary direction. For 3D velocimetry, a Hadamard scheme defines the polarities of velocity encoding gradients in three orthogonal directions. The phase graph shows that an echo in the echo train (black solid circles) is a mixture of SE based coherence pathways (gray solid lines, only lowest order coherence pathways are shown) and STE based coherence pathways (gray dashed lines, only lowest order coherence pathways are shown).

with the number of velocity encoding steps N_V (2 for 1D velocimetry and 4 for 3D velocimetry with the Hadamard scheme), and the gyromagnetic ratio γ. Note that for velocity encoding of slow liquid flow a large value of Δ is required considering the limited maximum gradient amplitude. The echo after the first refocusing pulse in the preparation module at $t = 2\tau$ (not shown in Fig. 1) will not be formed if the second velocity encoding gradient is not applied before $t = 2\tau$, and therefore this echo is not acquired. A subsequent RARE imaging module is used for fast spatial encoding. Pairs of balanced crusher gradients around all refocusing pulses are used to suppress unwanted coherence pathways.

Within each inter-refocusing interval, zeroth-order gradient moment nulling is applied by performing spatial decoding after spatial encoding and acquisition. This scheme suppresses image artifacts due to spin motions in the echo train, with only slightly increased minimum TE. Centric phase encoding is used for higher SNR and low T_2 contrast. Identical phase encoding gradients are applied within the inter-refocusing interval of an odd echo and the subsequent even echo, *i.e.* phase encoding gradients are incremented after every pair of odd and even echoes, in order to further compensate phase errors originating from the non-zero first-order gradient moments within each inter-refocusing interval. Detailed discussion about odd and even echoes will be given in Section 4.3. The effective TE for the MR images of the odd and even echoes are 4τ and 6τ, respectively.

Odd and even part of the real-valued propagator $P(\mathbf{R},\Delta)$ are the Fourier transform of the real and imaginary parts of the displacement-encoded complex-valued MR signals in the q-space domain (Re{S(**q**)} and Im{S(**q**)}), respectively [34]. Therefore, in both q-space MRI and phase contrast MRI, both of Re{S(**q**)} and Im{S(**q**)} shall be preserved and acquired correctly for velocimetry accuracy. However, S(**q**) will be distorted due to B_1 inhomogeneity, particularly in the RARE echo train. Re{S(**q**)} and Im{S(**q**)} can be separated by a pair of RF pulses within a two-step phase cycle [34], leading to a 50% signal loss due to the STE based filtering.

Another strategy is to apply a two-step phase cycling, where CPMG and CP RF pulse trains are used within the first and second phase cycling steps, respectively [33,36]. In the first phase cycling step, Re{S(**q**)} is preserved and Im{S(**q**)} is distorted in the CPMG pulse trains. On the contrary, in the second phase cycling step, Im{S(**q**)} is preserved and Re{S(**q**)} is distorted in the CP pulse trains. Since Im{S(**q**)} in the CPMG pulse trains is distorted with the same factor as Re{S(**q**)} in the CP pulse trains, the correct phase of S(**q**) can be recovered from the averaged signals within the two phase cycling steps.

One can also apply an imbalance in the read-dephasing gradient to separate SE based and STE based echoes in each inter-refocusing interval [46]. The mixing of SE and STE based echoes originates from B_1 inhomogeneity and results in a distortion of S(**q**). With a balanced read-dephasing gradient, SE and STE based echoes coincide. With an unbalanced read-dephasing gradient (typically one half of the balanced one), both parity echoes can be separated in the time domain. The combination of them can recover the information loss of the encoded displacements. This strategy does not need phase cycling and is thus at least twice as fast as the other two strategies mentioned above, though with the drawback of prolonged minimum TE and additional T_2^* contrast.

Table 1
The Hadamard scheme defining the polarities of velocity encoding gradients in 3D velocimetry.

Scan number	G_X	G_Y	G_Z
1	−	−	−
2	+	+	−
3	+	−	+
4	−	+	+

In this work, the two-step CPMG-CP phase cycling scheme [33,36] was used to achieve high SNR and reduced T_2^* contrast, which is essential for MRV in porous systems (*cf.* Fig. 1). To compensate for B_1 inhomogeneity, an additional phase shift of π is applied to the refocusing pulses for the odd echoes. Unlike in earlier publications [33,36], both odd and even echoes are acquired and combined to improve the SNR and velocimetry accuracy. A detailed discussion about the echo combination will be given in Section 4.3.

Gradient imperfections, such as eddy currents [39,40] and concomitant magnetic fields [41], can generate additional phase errors, leading to non-zero phase contrast for static spins as offsets. The velocity offset maps can be measured with zero flow (*i.e.* with the pump switched off) for correction of velocity maps.

Thus, the total measurement time T_{total} is given by

$$T_{total} = TR \cdot \frac{N_P}{N_{RARE}} \cdot N_S \cdot N_A \cdot N_V \cdot 2, \tag{2}$$

where N_P is the number of primary phase encoding steps, N_{RARE} is the RARE factor, N_S is the number of slices for 2D imaging (1 for multi-slice scheme) or the number of secondary phase encoding steps for 3D imaging, N_A is the number of averages (at least 2 for phase cycling), and the factor of 2 refers to the measurements performed with the pump switched on and off. The effective acceleration factor of the pulse sequence is one half of N_{RARE}, which is due to the used two-step phase cycling. Thus, with an $N_{RARE} > 2$, the pulse sequence reduces the minimum T_{total} as compared to a single SE pulse sequence.

2.4. Data post-processing

Data post-processing was performed by home-made programs written in Matlab R2014a (The MathWorks Inc., USA):

1. Individual MR raw datasets of odd and even echoes measured with the pump switched on and off in different velocity encoding steps were separately Fourier transformed, yielding complex-valued MR images.
2. Magnitude maps of the complex-valued MR images were averaged to generate the structural images.
3. By thresholding the MR images obtained in step 2, a binary mask was empirically determined and used in step 6 for nulling velocities in image background.
4. Phase contrast maps between the complex-valued MR images in different velocity encoding steps were calculated by complex conjugation instead of direct phase difference, avoiding additional phase wrapping.
5. Phase unwrapping was performed by calling the external function PRELUDE (FSL 5.0, University of Oxford, UK) [47] for individual phase contrast maps of odd and even echoes measured with the pump switched on and off.
6. Phase contrast maps were converted to velocity maps by multiplying the factor of VENC/π and the binary mask generated in step 3.
7. Echo-combined velocity maps were computed by voxel-wise averaging of velocity maps of odd and even echoes. Offset-corrected velocity maps were computed by voxel-wise subtraction of velocity maps measured with the pump switched off from velocity maps measured with the pump switched on.
8. Slice-wise VFR along a given direction was computed by integrating the corresponding velocity components in the direction and then multiplying by the cross-sectional area of a single voxel. For instance, slice-wise VFR along Z-axis ($VFR_Z(z)$) is given by

$$VFR_Z(z) = (L_X \cdot L_Y) \cdot \sum_{x,y} V_Z(x,y,z), \tag{3}$$

where L_X and L_Y are the voxel size in X- and Y-directions, respectively, and V_Z is the Z-component of the velocity.

9. Quantitative assessment of the proposed method, particularly the performance of echo combination and offset correction, is based on statistics of slice-wise VFR. On one hand, an averaged VFR over slices closest to the expected value of the pumping rate indicates the most accurate velocimetry. On the other hand, a least STD between VFR over slices implies the flow continuity.

2.5. Experimental procedure

First, the pulse sequence was implemented and examined by using the commercial RF coil. Due to limited vertical space available in the scanner bore, the filtration cell was placed horizontally at the coil center. The pumping rate was 12.6 mm^3/s, yielding a longitudinal flow through the filtration cell with velocities of up to 5 mm/s. Multi-slice 2D imaging with 1D velocimetry was performed. The measurement protocol was as follows: hermite RF pulses, τ 5.0 ms, effective TE 20.0/ 30.0 ms (odd/ even echo), FOV 20×20 mm^2, matrix size 160×160, read direction along X-axis, N_{RARE} 16, echo train length 330.0 ms, slice thickness 0.5 mm, number of slices 5, inter-slice distance 6.0 mm, slice direction along Z-axis, voxel size $0.125 \times 0.125 \times 0.5$ mm^3, Δ 10.0 ms, VENC 7.5 mm/s, 1D velocity encoding along Z-axis, N_V 2, TR 5.0 s, N_A 2, T_{total} 6.7 min.

Second, after the above examination, the pulse sequence was used in combination with the home-made RF coil. The filtration cell was placed vertically, with the sample at the coil center. The pumping rate was set to be 37.8 mm^3/s, providing a vertical flow through the filtration cell with velocities of up to 15 mm/s. 3D imaging with 1D velocimetry was performed. The measurement protocol was as follows: rectangular RF pulses, τ 4.0 ms, effective TE 16.0/ 24.0 ms (odd/ even echo), FOV $32 \times 16 \times 16$ mm^3, matrix size $200 \times 100 \times 100$, voxel size $0.160 \times 0.160 \times 0.160$ mm^3, read direction along Y-axis, RARE phase encoding direction along Z-axis, N_{RARE} 10, echo train length 168.0 ms, Δ 4.0 ms, VENC 15.0 mm/s, 1D velocity encoding along Y-axis, N_V 2, TR 1.0 s, N_A 2, T_{total} 2.2 h.

Third, 3D velocity maps of slow water flow through the filtration cell were acquired by using the home-made RF coil, mimicking the desired MRV application for deep bed filtration. The pumping rate was 12.6 mm^3/s, yielding a vertical flow through the filtration cell with velocities of up to 5 mm/s. The measurement protocol of the 3D imaging with 3D velocimetry was as follows: rectangular RF pulses, τ 4.0 ms, effective TE 16.0/ 24.0 ms (odd/ even echo), FOV $32 \times 16 \times 16$ mm^3, matrix size $200 \times 100 \times 100$, voxel size $0.160 \times 0.160 \times 0.160$ mm^3, read direction along Y-axis, RARE phase encoding direction along Z-axis, N_{RARE} 10, echo train length 168.0 ms, Δ 8.0 ms, VENC 5.0 mm/s, 3D velocity encoding along X-, Y- and Z-axes, N_V 4, TR 1.0 s, N_A 2, T_{total} 4.4 h.

3. Results

3.1. Examining the pulse sequence

MR images of distilled water in the sample (slice 2–4) and also in the outlet (slice 1) and inlet (slice 5) are shown in Fig. 2. The half ring structure outside the outlet in slice 1 is due to static water within the sealing of the filtration cell. The static water settled accidentally during the installation of the sample into the filtration cell. Since the sealing has no connection to the internal part of the filtration cell, the static water was considered to have no influences on the velocimetry results.

Nine velocity maps of the central slice (slice 3 in Fig. 2) are shown in Fig. 3, representing intermediate post-processing results

with echo combination and/or offset correction (*cf.* step 6 and 7 in Section 2.4). In the middle column, non-zero velocity maps of odd and even echoes alone and echo combination measured with the pump switched off can be observed, indicating the necessity of offset correction.

These nine velocity maps were compared by investigating the slice-wise longitudinal VFR (VFR_Z) (*cf.* step 8 in Section 2.4), as shown in Fig. 4. The best agreement with the expected VFR_Z (the pumping rate, gray dashed line in Fig. 4) is found if both echo combination and offset correction (black solid bars in Fig. 4) are applied. Statistics of VFR_Z over *XY*-slices (*cf.* step 9 in Section 2.4), as shown in Table 2, also support this finding: with both echo combination and offset correction, the averaged VFR_Z over *XY*-slices has the most accurate value (13.1 mm^3/s compared to 12.6 mm^3/s corresponding to the pumping rate, relative error 3.97%) and the STD between VFR_Z over *XY*-slices has the least value (1.00 mm^3/s).

3.2. 3D imaging with 1D velocimetry

An MR image of distilled water in the filtration cell is shown in Fig. 5a. Reduced image intensities were observed in the inlet (top region) and outlet (bottom region), resulting from the B_1 inhomogeneity of the coil (*cf.* Section 2.5). In the bottom right region in Fig. 5a, again some static water within the sealing of the filtration cell is visible, as described in Section 3.1.

The vertical velocity (V_Y) map after echo combination and offset correction (Fig. 5b) shows several main streaming paths of the distilled water through the sample. The negative values stand for velocities in -*Y* direction, *i.e.* vertically downwards.

Vertical VFR (VFR_Y) values versus *XZ*-slice position are plotted in Fig. 5c. Large linear ramps of VFR and thus velocities are found in the datasets measured with the pump switched on (gray solid lines with up triangle, down triangle and rectangle markers in Fig. 5c) and off (gray solid lines with left triangle, right triangle and diamond markers in Fig. 5c), respectively. With offset correction, these ramps are substantially compensated (gray solid lines with asterisk and hexagonal star markers, and black solid line with circle markers in Fig. 5c). Afterwards, echo combination (black solid line with circle markers in Fig. 5c) yields a VFR_Y which is in better agreement with the pumping rate (black dashed line in Fig. 5c) than those obtained from odd (gray solid lines with asterisk markers in Fig. 5c) or even (gray solid lines with hexagonal star markers in Fig. 5c) echoes alone.

Statistics of VFR_Y over *XZ*-slices (*cf.* step 9 in Section 2.4) are shown in Table 3. Fluctuations of velocities can be strongly reduced by offset correction. Additionally, systematic errors are substantially reduced by echo combination, yielding an accurate averaged VFR_Y of -36.6 mm^3/s compared to -37.8 mm^3/s (relative error 3.28%) corresponding to the pumping rate, although with slightly higher STD of 1.62 mm^3/s than for the dataset of the odd echo of 1.02 mm^3/s (*cf.* 4th column in Table 3).

3.3. 3D imaging with 3D velocimetry

An MR image with overlaid velocity vector fields of the central *XY*-slice with an enlarged view of an image section (black rectangle) are shown in Fig. 6a. The vertical VFR (VFR_Y) values versus *XZ*-slice position are plotted in Fig. 6b, yielding consistent VFR_Y (solid line in Fig. 6b) slightly lower than expected (dashed line in Fig. 6b). Similarly, Fig. 6c shows an MR image with overlaid velocity vector fields of the central *XZ*-slice, with an enlarged view of an image section (black rectangle). As an example of the transversal VFR, the VFR along the *X*-axis (VFR_X) versus *YZ*-slice position are plotted in Fig. 6d. The fluctuations of the slice-wise VFR_X around

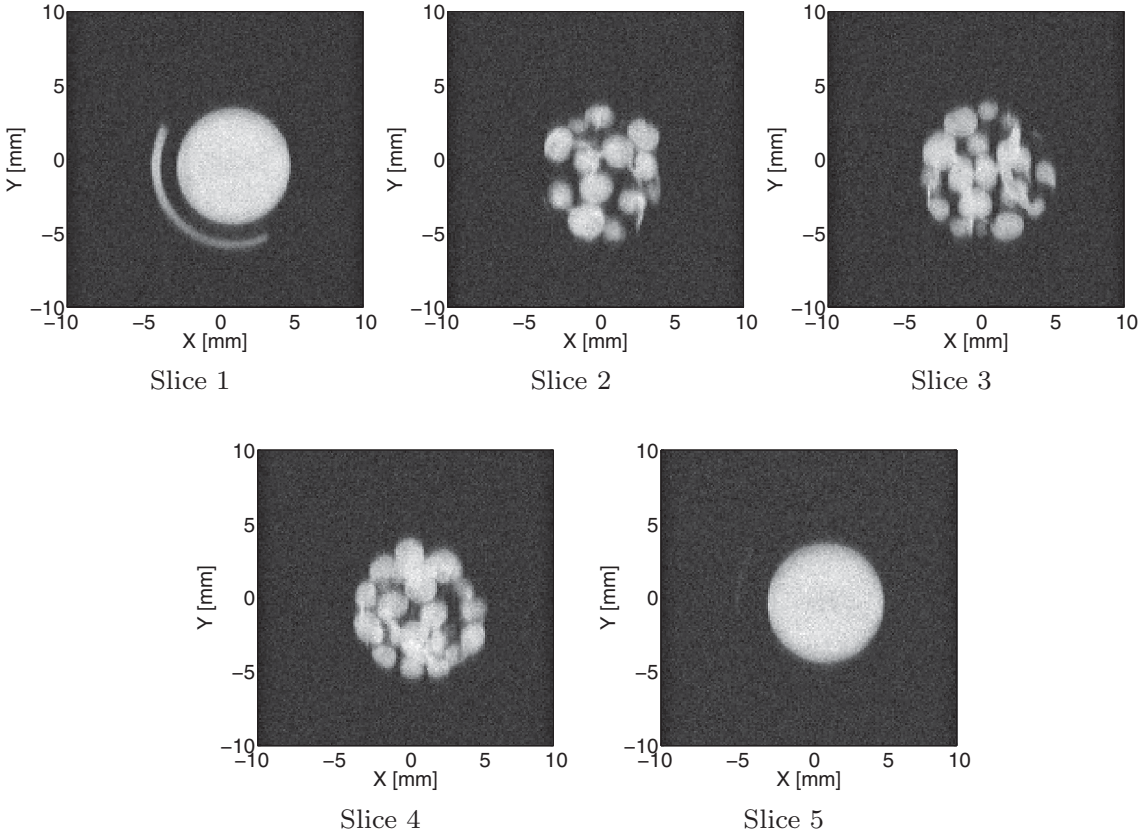

Fig. 2. MR images of 5 slices in the 2D imaging with 1D velocimetry measurement. Slice 1 is in the outlet, slice 2–4 in the sample, and slice 5 in the inlet.

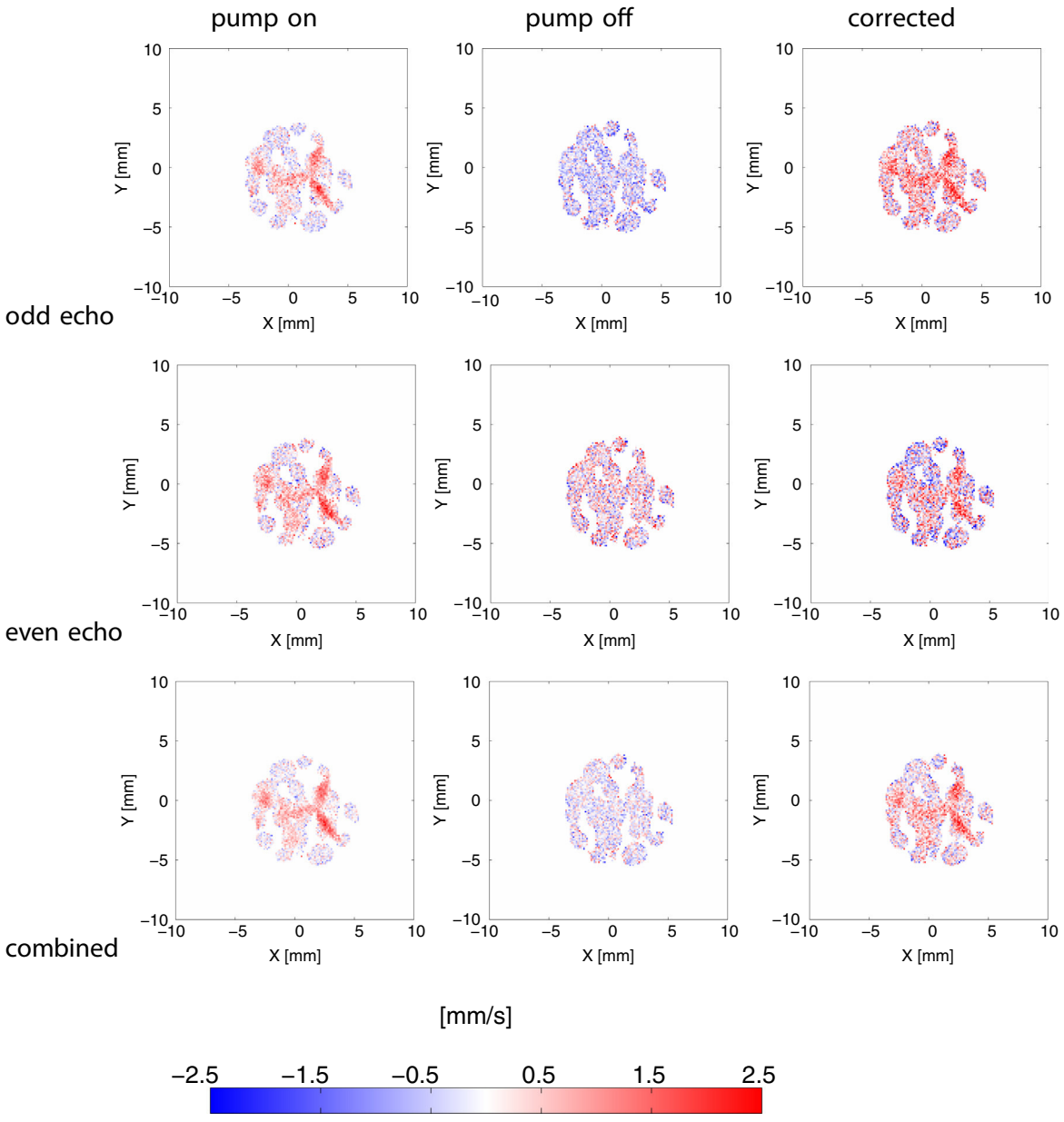

Fig. 3. Velocity maps of the central slice (slice 3 in Fig. 2) in the 2D imaging with 1D velocimetry measurement as intermediate post-processing results with echo combination and/or offset correction (*cf.* step 6 and 7 in Section 2.4).

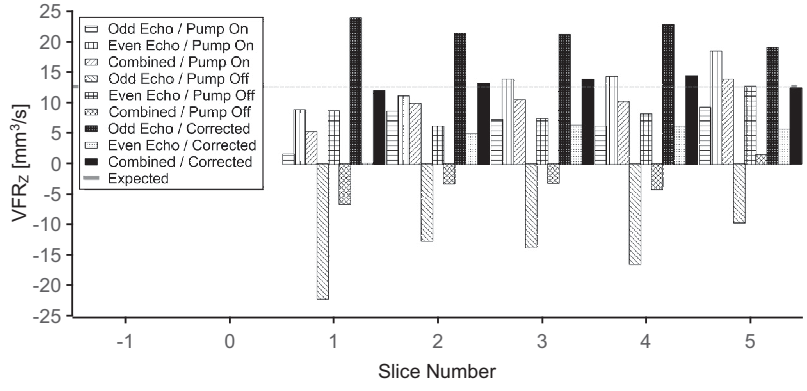

Fig. 4. Bar graph of slice-wise longitudinal VFR (VFR_Z) calculated from nine velocity maps (*cf.* step 8 in Section 2.4) in the 2D imaging with 1D velocimetry measurement. These maps represent intermediate post-processing results with echo combination and/or offset correction (*cf.* step 6 and 7 in Section 2.4).

Table 2
Statistics (average ± STD, *cf.* step 9 in Section 2.4) of longitudinal VFR (VFR_Z) over *XY*-slices in the 2D imaging with 1D velocimetry measurement.

VFR_Z [mm^3/s]	Pump on	Pump off	Corrected
Odd echo	6.59 ± 3.03	−15.1 ± 4.71	21.7 ± 1.81
Even echo	13.3 ± 3.62	8.63 ± 2.49	4.65 ± 2.57
Combined	9.93 ± 3.08	−3.22 ± 3.00	13.1 ± 1.00

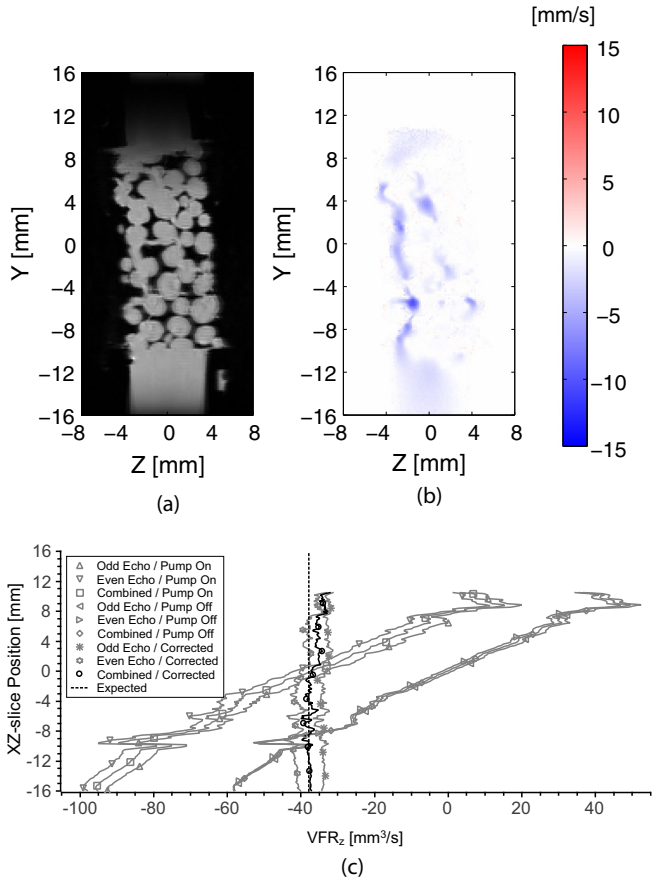

Fig. 5. Results of the 3D imaging with 1D velocimetry measurement. (a) MR image of the central *YZ*-slice. (b) Vertical velocity (V_Y) map of the central *YZ*-slice. (c) Plot of vertical VFR (VFR_Y) values versus *XZ*-slice position.

Table 3
Statistics (average ± STD, *cf.* step 9 in Section 2.4) of vertical VFR (VFR_Y) over *XZ*-slices in the 3D imaging with 1D velocimetry measurement.

VFR_Z [mm^3/s]	Pump on	Pump off	Corrected
Odd echo	−42.9 ± 33.5	−9.36 ± 32.9	−33.6 ± 1.02
Even echo	−51.3 ± 33.7	−11.6 ± 31.7	−40.0 ± 2.39
Combined	−47.1 ± 33.6	−10.5 ± 32.3	−36.6 ± 1.62

zero (*cf.* Fig. 6d) reflect that no net transversal flow or leakage was taking place during the measurement. The averaged VFR_Y with STD over *XZ*-slices is -12.0 ± 0.524 mm^3/s compared to -12.6 mm^3/s (relative error 4.76%) corresponding to the pumping rate, while the averaged VFR_X with STD over *YZ*-slices is 0.139 ± 0.780 mm^3/s compared to the expected zero value, respectively.

4. Discussion

In this work, both the experimental setup and existing MRV methods were optimized for velocimetry of slow liquid flow in porous media. First, a dedicated RF coil was constructed and adjusted to the specific requirements of a filtration cell used to study deep bed filtration. Second, a RARE phase contrast MRI pulse sequence was modified for fast and accurate velocimetry in porous media despite B_1 inhomogeneity, particularly by means of offset correction and echo combination. Third, a set of supplementary routines for data post-processing was used to quantify and verify velocity fields measured in a porous sample.

4.1. Pulse sequence acceleration

Acceleration of the pulse sequence is determined by the factor N_{RARE} that depends on the inter-echo delay and the maximum echo train length, which is in turn restricted by the T_2 signal decaying. The pulse sequence proved to be insensitive to phase errors introduced by certain intra- and inter-pore displacements in the echo train, resulting in accurate velocity maps and suppressed displacement-related blurring and ghosting artifacts. This can be examined particularly in the 3D imaging with 1D velocimetry experiment with a pumping rate of 37.8 mm^3/s, which is three times higher than in the other experiments (12.6 mm^3/s). The moving spins with the velocity range of [−15,15] mm/s have the displacements of up to 2.52 mm after the echo train, which are equivalent to up to 15.75 voxels with the voxel size of 0.160 mm and 1.26 pores with the pore size of about 2 mm.

Under the assumption of negligible velocity changes of moving spins in the echo train, suppression of the displacement-related phase errors is achieved by four means: (i) read dephasing, acquisition and read rephasing within each inter-refocusing interval, suppressing phase errors in read direction; (ii) identical pairs of phase encoding winder and rewinder gradients for each pair of odd and even echoes, compensating phase errors in phase encoding direction after an even number of echoes; (iii) balanced crusher gradient pairs, canceling out displacement-introduced phase errors in slice direction after an even number of echoes; (iv) centric phase encoding, minimizing displacements during the delay between velocity encoding and the subsequent first pair of odd and even echoes, when the central *k-space* region is acquired (24 ms and thus displacements of up to 0.18 pores in the 3D imaging with 1D velocimetry experiment).

However, for very fast flow, even during the delay between velocity encoding and the subsequent acquisition of the central k-space region, moving spins will have very large inter-pore displacements and altered velocities, thus preventing accurate velocimetry by the pulse sequence.

For systems with negligible changes in B_0 fields during a series of *in situ* MRV measurements with a fixed protocol, each MRV measurement only takes $T_{total}/2$ as the real measurement time, since the velocity offset maps can be regarded as consistent and require only one additional *in situ* MRV measurement with the identical protocol.

4.2. Offset correction

The necessity of the applied offset correction for accurate velocimetry is shown by the non-zero velocities measured with the pump switched off in the 2D imaging with 1D velocimetry experiment (middle column in Fig. 3). According to the slice-wise longitudinal VFR (VFR_Z, dashed lines with triangle markers in Fig. 4) as well as the averaged VFR_Z with STD over *XY*-slices (3rd column in Table 2), phase contrast is introduced for static spins by inverting the polarity of velocity encoding gradients. The same was found in the 3D imaging with 1D velocimetry experiment, where the ramp of slice-wise vertical VFR (VFR_Y) is only compensated after offset correction (Fig. 5c and Table 3). This additional phase contrast most likely originates from gradient imperfections, such as eddy currents [39,40] and concomitant fields [41]. There-

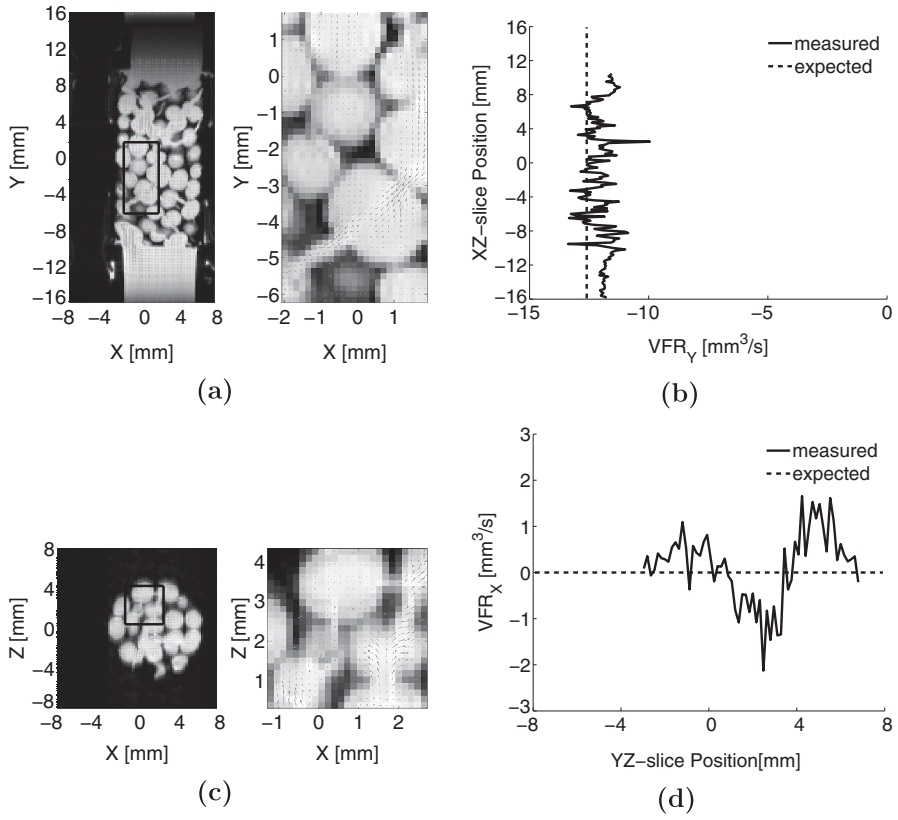

Fig. 6. Results of the 3D imaging with 3D velocimetry measurement. (a) MR image with overlaid velocity vector fields of the central *XY*-slice, and an example enlarged view of image section (black rectangle). (b) Plot of vertical VFR (VFR_Y) versus *XZ*-slice position. (d) MR image with overlaid velocity vector fields of the central *XZ*-slice, and an example enlarged view of image section (black rectangle). (d) Plot of transveral VFR along *X*-axis (VFR_X) versus *YZ*-slice position.

fore, for fixed B_0 fields and a given measurement protocol, it will remain unchanged when performing measurements with the pump switched either on or off, thus enabling precise velocity maps by offset correction.

4.3. Echo combination

The assessment between odd and even echoes alone and echo combination was performed by comparing slice-wise longitudinal VFR (VFR_Z) and averaged VFR_Z with STD over *XY*-slices in the 2D imaging with 1D velocimetry experiment (black solid bars in Fig. 4, and 4th column in Table 2), and also slice-wise vertical VFR (VFR_Y) and averaged VFR_Y with STD over *XZ*-slices in the 3D imaging with 1D velocimetry experiment (black solid line with circle markers in Fig. 5c, and 4th column in Table 3). Echo combination was superior in velocimetry accuracy to using odd or even echoes alone, giving best agreement with the expected VFR (12.6 mm^3/s, gray dashed line in Fig. 4, and 37.8 mm^3/s, black dashed line in Fig. 5c).

The echo combination strategy was validated by MRV measurements of the simple laminar flow of distilled water in a tube using the commercial RF coil with high B_1 homogeneity. The measured flow patterns, which were acquired by the proposed RARE MRV approach and a single SE phase contrast MRI pulse sequence, show good agreements with each other and also coincide with the parabolic flow pattern expected for the given pumping rate (*cf.* supplementary material 2).

The mechanisms of echo combination may be explained as follows. Due to the balanced pairs of crusher gradients, free induction decays are suppressed and each detected echo is a mixture of SE based and STE based coherence pathways (*cf.* Fig. 1, phase graph). The discussion here focuses on the lowest order SE based coherence pathway CP_{SE} and STE based coherence pathway CP_{STE}, which are main contribution to the echoes. CP_{SE} represents the pulse train of $\pi/2 - \pi - [\pi]_{n-1} - \pi$, while CP_{STE} represents the pulse train of $\pi/2 - \pi - [\pi]_{n-2} - \pi/2 - \pi/2$. Details of coherence pathways can be found in [48–51]. The main difference between both is that CP_{STE} experiences no gradients in the preceding inter-refocusing interval, while CP_{SE} experiences gradients in the preceding inter-refocusing interval. For an odd echo, CP_{SE} experiences both zeroth- and first-order gradient moment nulling, due to an even number of pairs of phase encoding winder and rewinder gradients, an even number of pairs of crusher gradients, and an even number of refocusing pulses with existing internal magnetic field gradients. Therefore, CP_{SE} has no additional displacement-introduced phase contrast. However, without experiencing gradients in the preceding inter-refocusing interval, CP_{STE} has additional phase contrast due to non-zero first-order gradient moments. The opposite situation is found for the subsequent even echo, while only CP_{STE} instead of CP_{SE} experiences first-order gradient moment nulling. The additional phase contrast due to non-zero first-order gradient moments occur only in CP_{SE} instead of CP_{STE}. The combination of odd and even echoes is used to suppress the additional phase contrast for both coherence pathways.

It is noteworthy that velocimetry accuracy was far more improved by echo combination in the 2D imaging with 1D velocimetry experiment than in the 3D imaging with 1D velocimetry experiment. Odd or even echoes alone generated totally incorrect VFR in the former experiment (black bars with white dots and white bars with black dots in Fig. 4, and 4th column in Table 2), and yielded approximately correct VFR in the latter experiment (gray solid lines with asterisk and hexagonal star markers in Fig. 5c,

and 4th column in Table 3). The same finding was observed in MRV measurements of the simple laminar flow of distilled water in a tube using the commercial RF coil (*cf.* supplementary material 2). This difference may be due to additional phase contrast originating from the slice-selection and slice-rephasing gradients, which are not discussed above. These gradients were not applied in the non-slice-selective 3D imaging experiment, but had high amplitudes in the 2D imaging experiment in order to achieve thin slices. Two types of undesired additional phase contrast into odd and even echoes were then introduced. Except for the first slice-selection gradient with the excitation pulse, the other slice-selection gradients produced the first type of additional phase contrast. Similar to the discussion for crusher gradients and internal magnetic field gradients above, this additional phase contrast can be suppressed by echo combination. The second type of additional phase contrast resulted from the first slice-selection and slice-rephasing gradients. This phase contrast had inverse polarity within the odd and even echoes in both SE and STE based coherence pathways, and thus can be compensated by echo combination. As a result, in both 2D and 3D imaging experiments, consistent and correct VFR were obtained from offset-corrected and echo-combined velocity maps.

4.4. Data post-processing

Because of the velocity offsets, phase wrapping can still occur even if the real velocity value is within the velocity encoding range. A considerably large VENC, particularly with small velocity encoding gradient amplitude, can eliminate phase wrapping. However, since the velocity STD is proportional to VENC [24–26], an appropriate VENC, which is only slightly larger than the maximum real velocity value, is preferred, making phase unwrapping necessary. Moreover, it can rescue measurements for which detailed prior knowledge of the velocity distribution in tortuous structures is not available.

In this work, the quantitative analysis of flow was based on slice-wise VFR values, which were obtained by integrating velocities within voxels in the same slices (*cf.* step 8 in Section 2.4). Errors may occur within voxels at interfaces between liquid and porous media, since these voxels are only partially filled with liquid. In this work, however, the spatial resolution was very high ($0.125^2 \times 0.5\,mm^3$ in 2D and $0.160^3\,mm^3$ in 3D imaging experiments), *i.e.* the voxel size was much smaller than the mean pore size of about 2 mm. Thus, the partial volume effects were regarded as negligible. This integration was examined by MRV measurements of the simple laminar flow of distilled water in a tube using the commercial RF coil. The VFR values calculated by integration agree with the VFR values calculated by parabolic fitting (*cf.* supplementary material 2).

In the future, computational fluid dynamics studies can be performed based on the detailed knowledge on the porous structures, which can be acquired by MRI or X-ray μCT. This will allow a cross-validation between the simulated velocity fields and the velocity maps measured by the proposed MRV approach.

5. Conclusion

In this work, an optimized RARE based MRV method is proposed to achieve fast, robust and accurate velocity mapping for slow liquid flow in porous media. MRV measurements of slow liquid flow in porous media within a horizontal magnet are enabled by using pulse sequence modification, particularly the combined use of odd and even echoes and an adjusted RF coil. While this approach was primarily developed for studies on deep bed filtration, it may also be of interest for other MRV studies.

Acknowledgement

This work was supported by German Research Foundation within the Research Training Group GRK 1860 "Micro-, meso- and macroporous nonmetallic Materials: Fundamentals and Applications" (MIMENIMA). We acknowledge Martin Nowak in the Workshop of Faculty 02, University of Bremen for his help during the RF coil construction, and our colleague Dr. Peter Erhard for helpful comments on the manuscript.

Appendix A. Supplementary material

Supplementary data associated with this article can be found, in the online version, at http://dx.doi.org/10.1016/j.jmr.2017.01.017.

References

[1] K.-M. Yao, M. Habibian, C. O'Melia, Water and waste water filtration: concepts and applications, Environ. Sci. Technol. 5 (11) (1971) 1105–1112, http://dx.doi.org/10.1021/es60058a005.

[2] K. Ives (Ed.), The Scientific Basis of Filtration: Proceedings of the NATO Advanced Study Institute on the Scientific Basis of Filtration held at Cambridge, UK, July 2–20, 1973, vol. 2, Noordhoff Leyden, 1975.

[3] L. McDowell-Boyer, J. Hunt, N. Sitar, Particle transport through porous media, Water Resour. Res. 22 (13) (1986) 1901–1921, http://dx.doi.org/10.1029/WR022i013p01901.

[4] K. Sutherland, Filters and Filtration Handbook, 5th ed., Elsevier Science, 2008.

[5] A. de Haan, H. Bosch, Industrial Separation Processes: Fundamentals, De Gruyter, 2013.

[6] F. Al-Abduwani, R. Farajzadeh, W. van den Broek, P. Currie, P. Zitha, Filtration of micron-sized particles in granular media revealed by x-ray computed tomography, Rev. Sci. Instrum. 76 (10). http://dx.doi.org/10.1063/1.2103467.

[7] X. Li, C.-L. Lin, J. Miller, W. Johnson, Pore-scale observation of microsphere deposition at grain-to-grain contacts over assemblage-scale porous media domains using X-ray microtomography, Environ. Sci. Technol. 40 (12) (2006) 3762–3768, http://dx.doi.org/10.1021/es0525004.

[8] J.-F. Gaillard, C. Chen, S. Stonedahl, B. Lau, D. Keane, A. Packman, Imaging of colloidal deposits in granular porous media by X-ray difference microtomography, Geophys. Res. Lett. 34 (18) (2007) L18404, http://dx.doi.org/10.1029/2007GL030514.

[9] C. Chen, B. Lau, J.-F. Gaillard, A. Packman, Temporal evolution of pore geometry, fluid flow, and solute transport resulting from colloid deposition, Water Resour. Res. 45 (6) (2009) W06416, http://dx.doi.org/10.1029/2008WR007252.

[10] X. Li, Z. Li, D. Zhang, Role of low flow and backward flow zones on colloid transport in pore structures derived from real porous media, Environ. Sci. Technol. 44 (13) (2010) 4936–4942, http://dx.doi.org/10.1021/es903647g.

[11] W. Long, H. Huang, J. Serlemitsos, E. Liu, A. Reed, M. Hilpert, Pore-scale study of the collector efficiency of nanoparticles in packings of nonspherical collectors, Colloids Surf. A 358 (1–3) (2010) 163–171, http://dx.doi.org/10.1016/j.colsurfa.2010.01.043.

[12] Z. Li, D. Zhang, X. Li, Tracking colloid transport in real pore structures: comparisons with correlation equations and experimental observations, Water Resour. Res. 48 (5) (2012) W05533, http://dx.doi.org/10.1029/2012WR011847.

[13] A. Waske, M. Heiland, S. Odenbach, Local position of colloid clusters in a packed bed of spheres, Chem. Eng. Sci. 76 (2012) 192–198, http://dx.doi.org/10.1016/j.ces.2012.04.034.

[14] S. Günther, S. Odenbach, A method for image decomposition and particle quantification in multiphase systems, Transp. Porous Media 112 (1) (2016) 105–116, http://dx.doi.org/10.1007/s11242-016-0634-x.

[15] C. Dirckx, S. Clark, L. Hall, B. Antalek, J. Tooma, J. Hewitt, K. Kawaoka, Magnetic resonance imaging of the filtration process, AIChE J. 46 (1) (2000) 6–14, http://dx.doi.org/10.1002/aic.690460103.

[16] F. Heese, J. Acosta-Cabronero, P. Robson, L. Hall, Measurement of particle separation by magnetic resonance imaging, IEEE Sens. J. 5 (2) (2005) 268–272, http://dx.doi.org/10.1109/JSEN.2005.843898.

[17] S. Buetehorn, L. Utiu, M. Küppers, B. Blümich, T. Wintgens, M. Wessling, T. Melin, NMR imaging of local cumulative permeate flux and local cake growth in submerged microfiltration processes, J. Membr. Sci. 371 (1–2) (2011) 52–64, http://dx.doi.org/10.1016/j.memsci.2011.01.018.

[18] C. Elkins, M. Alley, Magnetic resonance velocimetry: applications of magnetic resonance imaging in the measurement of fluid motion, Exp. Fluids 43 (6) (2007) 823–858, http://dx.doi.org/10.1007/s00348-007-0383-2.

[19] L. Gladden, A. Sederman, Recent advances in flow MRI, J. Magn. Reson. 229 (2013) 2–11, http://dx.doi.org/10.1016/j.jmr.2012.11.022.

[20] P. Callaghan, C. Eccles, Y. Xia, NMR microscopy of dynamic displacements: k-space and q-space imaging, J. Phys. E: Sci. Instrum. 21 (8) (1988) 820, http://dx.doi.org/10.1088/0022-3735/21/8/017.

[21] P. Moran, A flow velocity zeugmatographic interlace for NMR imaging in humans, Magn. Reson. Imaging 1 (4) (1982) 197–203, http://dx.doi.org/10.1016/0730-725X(82)90170-9.
[22] D. Bryant, J. Payne, D. Firmin, D. Longmore, Measurement of flow with NMR imaging using a gradient pulse and phase difference technique, J. Comput. Assist. Tomogr. 8 (4) (1984) 588–593, http://dx.doi.org/10.1097/00004728-198408000-00002.
[23] P. Moran, R. Moran, N. Karstaedt, Verification and evaluation of internal flow and motion: true magnetic resonance imaging by the phase gradient modulation method, Radiology 154 (2) (1985) 433–441, http://dx.doi.org/10.1148/radiology.154.2.3966130.
[24] T. Conturo, G. Smith, Signal-to-noise in phase angle reconstruction: dynamic range extension using phase reference offsets, Magn. Reson. Med. 15 (3) (1990) 420–437, http://dx.doi.org/10.1002/mrm.1910150308.
[25] M. Bernstein, Y. Ikezaki, Comparison of phase-difference and complex-difference processing in phase-contrast MR angiography, J. Magn. Reson. Imaging 1 (6) (1991) 725–729, http://dx.doi.org/10.1002/jmri.1880010620.
[26] N. Pelc, F. Sommer, K. Li, T. Brosnan, R. Herfkens, D. Enzmann, Quantitative magnetic resonance flow imaging, Magn. Reson. Q. 10 (3) (1994) 125–147.
[27] J. Hennig, A. Nauerth, H. Friedburg, RARE imaging: a fast imaging method for clinical MR, Magn. Reson. Med. 3 (6) (1986) 823–833, http://dx.doi.org/10.1002/mrm.1910030602.
[28] T. Scheenen, D. van Dusschoten, P. de Jager, H. van As, Microscopic displacement imaging with pulsed field gradient turbo SpinEcho NMR, J. Magn. Reson. 142 (2) (2000) 207–215, http://dx.doi.org/10.1006/jmre.1999.1916.
[29] T. Scheenen, F. Vergeldt, C. Windt, P. de Jager, H. van As, Microscopic imaging of slow flow and diffusion: a pulsed field gradient stimulated echo sequence combined with turbo spin echo imaging, J. Magn. Reson. 151 (1) (2001) 94–100, http://dx.doi.org/10.1006/jmre.2001.2362.
[30] A. Sederman, M. Mantle, L. Gladden, Single excitation multiple image RARE (SEMI-RARE): ultra-fast imaging of static and flowing systems, J. Magn. Reson. 161 (1) (2003) 15–24, http://dx.doi.org/10.1016/S1090-7807(02)00141-6.
[31] F. Casanova, J. Perlo, B. Blümich, K. Kremer, Multi-echo imaging in highly inhomogeneous magnetic fields, J. Magn. Reson. 166 (1) (2004) 76–81, http://dx.doi.org/10.1016/j.jmr.2003.09.008.
[32] A. Sederman, M. Mantle, C. Buckley, L. Gladden, MRI technique for measurement of velocity vectors, acceleration, and autocorrelation functions in turbulent flow, J. Magn. Reson. 166 (2) (2004) 182–189, http://dx.doi.org/10.1016/j.jmr.2003.10.016.
[33] P. Galvosas, P. Callaghan, Fast magnetic resonance imaging and velocimetry for liquids under high flow rates, J. Magn. Reson. 181 (1) (2006) 119–125, http://dx.doi.org/10.1016/j.jmr.2006.03.020.
[34] S. Ahola, J. Perlo, F. Casanova, S. Stapf, B. Blümich, Multiecho sequence for velocity imaging in inhomogeneous rf fields, J. Magn. Reson. 182 (1) (2006) 143–151, http://dx.doi.org/10.1016/j.jmr.2006.06.017.
[35] A. Amar, B. Blümich, F. Casanova, Rapid multiphase flow dynamics mapped by single-shot MRI velocimetry, ChemPhysChem 11 (12) (2010) 2630–2638, http://dx.doi.org/10.1002/cphc.201000062.
[36] S. Kuczera, P. Galvosas, Advances and artefact suppression in RARE-velocimetry for flow with curved streamlines, J. Magn. Reson. 259 (2015) 135–145, http://dx.doi.org/10.1016/j.jmr.2015.07.015.
[37] M. Shukla, A. Vallatos, V. Phoenix, W. Holmes, Accurate phase-shift velocimetry in rock, J. Magn. Reson. 267 (2016) 43–53, http://dx.doi.org/10.1016/j.jmr.2016.04.006.
[38] N. Spindler, P. Galvosas, A. Pohlmeier, H. Vereecken, NMR velocimetry with 13-interval stimulated echo multi-slice imaging in natural porous media under low flow rates, J. Magn. Reson. 212 (1) (2011) 216–223, http://dx.doi.org/10.1016/j.jmr.2011.07.004.
[39] P. Jehenson, M. Westphal, N. Schuff, Analytical method for the compensation of eddy-current effects induced by pulsed magnetic field gradients in NMR systems, J. Magn. Reson. 90 (2) (1990) 264–278, http://dx.doi.org/10.1016/0022-2364(90)90133-T.
[40] A. Caprihan, S. Altobelli, E. Benitez-Read, Flow-velocity imaging from linear regression of phase images with techniques for reducing eddy-current effects, J. Magn. Reson. 90 (1) (1990) 71–89, http://dx.doi.org/10.1016/0022-2364(90)90366-H.
[41] M. Bernstein, X. Zhou, J. Polzin, K. King, A. Ganin, N. Pelc, G. Glover, Concomitant gradient terms in phase contrast MR: analysis and correction, Magn. Reson. Med. 39 (2) (1998) 300–308, http://dx.doi.org/10.1002/mrm.1910390218.
[42] M. Adam, S. Kocanis, T. Fey, M. Wilhelm, G. Grathwohl, Hierarchically ordered foams derived from polysiloxanes with catalytically active coatings, J. Eur. Ceram. Soc. 34 (7) (2014) 1715–1725, http://dx.doi.org/10.1016/j.jeurceramsoc.2013.12.011.
[43] E. Insko, L. Bolinger, Mapping of the radiofrequency field, J. Magn. Reson., Ser. A 103 (1) (1993) 82–85, http://dx.doi.org/10.1006/jmra.1993.1133.
[44] C. Dumoulin, S. Souza, R. Darrow, N. Pelc, W. Adams, S. Ash, Simultaneous acquisition of phase-contrast angiograms and stationary-tissue images with hadamard encoding of flow-induced phase shifts, J. Magn. Reson. Imaging 1 (4) (1991) 399–404, http://dx.doi.org/10.1002/jmri.1880010403.
[45] N. Pelc, M. Bernstein, A. Shimakawa, G. Glover, Encoding strategies for three-direction phase-contrast MR imaging of flow, J. Magn. Reson. Imaging 1 (4) (1991) 405–413, http://dx.doi.org/10.1002/jmri.1880010404.
[46] G. Shiko, A. Sederman, L. Gladden, MRI technique for the snapshot imaging of quantitative velocity maps using RARE, J. Magn. Reson. 216 (2012) 183–191, http://dx.doi.org/10.1016/j.jmr.2012.01.021.
[47] M. Jenkinson, Fast, automated, N-dimensional phase-unwrapping algorithm, Magn. Reson. Med. 49 (1) (2003) 193–197, http://dx.doi.org/10.1002/mrm.10354.
[48] J. Hennig, Multiecho imaging sequences with low refocusing flip angles, J. Magn. Reson. 78 (3) (1988) 397–407, http://dx.doi.org/10.1016/0022-2364(88)90128-X.
[49] J. Hennig, Echoes – how to generate, recognize, use or avoid them in MR-imaging sequences. Part I: Fundamental and not so fundamental properties of spin echoes, Concepts Magn. Reson., Part A 3 (3) (1991) 125–143, http://dx.doi.org/10.1002/cmr.1820030302.
[50] J. Hennig, Echoes – how to generate, recognize, use or avoid them in MR-imaging sequences. Part II: Echoes in imaging sequences, Concepts Magn. Reson., Part A 3 (4) (1991) 179–192, http://dx.doi.org/10.1002/cmr.1820030402.
[51] K. Scheffler, A pictorial description of steady-states in rapid magnetic resonance imaging, Concepts Magn. Reson., Part A 11 (5) (1999) 291–304, doi:10.1002/(SICI)1099-0534(1999)11:5<291::AID-CMR2>3.0.CO;2-J.